(12) INTERNATIONAL APPLICATION PUBLISHED UNDER THE PATENT COOPERATION TREATY (PCT)

(19) World Intellectual Property Organization
International Bureau

(43) International Publication Date
27 November 2003 (27.11.2003)

PCT

(10) International Publication Number
WO 03/097291 A1

(51) International Patent Classification[7]: B23K 26/00

(21) International Application Number: PCT/US03/15701

(22) International Filing Date: 16 May 2003 (16.05.2003)

(25) Filing Language: English

(26) Publication Language: English

(30) Priority Data:
60/381,034 16 May 2002 (16.05.2002) US

(71) Applicant *(for all designated States except US)*: **THE TRUSTEES OF COLUMBIA UNIVERSITY IN THE CITY OF NEW YORK** [US/US]; 116th Street and Broadway, New York, NY 10027 (US).

(72) Inventors; and

(75) Inventors/Applicants *(for US only)*: **ZHANG, Wenwu** [CN/US]; 2150 Rosa Road, Hampshire House apt. C9C, Schenectady, NY 12309 (US). **YAO, Y., Lawrence** [US/US]; 560 Riverside Drive, Apt. 7J, New York, NY 10027 (US).

(74) Agents: **TANG, Henry** et al.; Baker Botts LLP, 30 Rockefeller Plaza, New York, NY 10112-4498 (US).

(81) Designated States *(national)*: AE, AG, AL, AM, AT, AU, AZ, BA, BB, BG, BR, BY, BZ, CA, CH, CN, CO, CR, CU, CZ, DE, DK, DM, DZ, EC, EE, ES, FI, GB, GD, GE, GH, GM, HR, HU, ID, IL, IN, IS, JP, KE, KG, KP, KR, KZ, LC, LK, LR, LS, LT, LU, LV, MA, MD, MG, MK, MN, MW, MX, MZ, NI, NO, NZ, OM, PH, PL, PT, RO, RU, SC, SD, SE, SG, SK, SL, TJ, TM, TN, TR, TT, TZ, UA, UG, US, UZ, VC, VN, YU, ZA, ZM, ZW.

(84) Designated States *(regional)*: ARIPO patent (GH, GM, KE, LS, MW, MZ, SD, SL, SZ, TZ, UG, ZM, ZW), Eurasian patent (AM, AZ, BY, KG, KZ, MD, RU, TJ, TM), European patent (AT, BE, BG, CH, CY, CZ, DE, DK, EE, ES, FI, FR, GB, GR, HU, IE, IT, LU, MC, NL, PT, RO, SE, SI, SK, TR), OAPI patent (BF, BJ, CF, CG, CI, CM, GA, GN, GQ, GW, ML, MR, NE, SN, TD, TG).

Published:
— *with international search report*
— *before the expiration of the time limit for amending the claims and to be republished in the event of receipt of amendments*

[Continued on next page]

(54) Title: METHODS FOR MICROSCALE LASER SHOCK PROCESSING OF METAL THIN FILMS

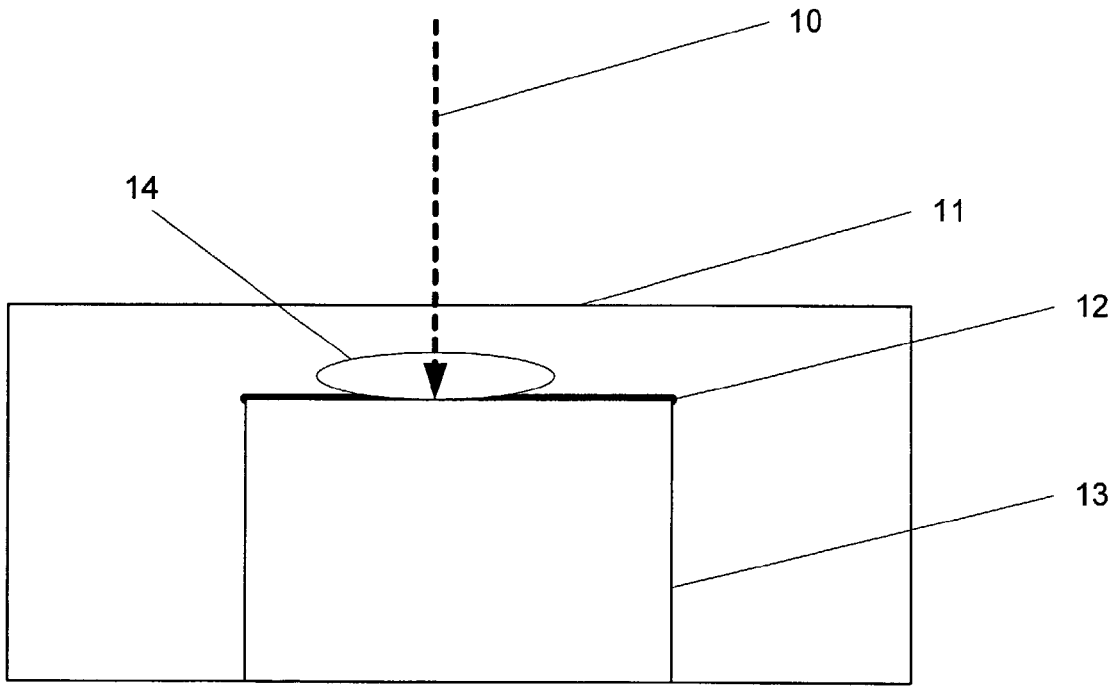

(57) Abstract: The present invention relates to techniques for microscale shock processing (LSP), in particular relating to processing of thin metal films which increases the reliability of metal used in applications such as micro-electromechanical structures (MEMS). The present invention includes methods for modeling and characterization in connection with microscale LSP of tin metal films.

WO 03/097291 A1

For two-letter codes and other abbreviations, refer to the "Guidance Notes on Codes and Abbreviations" appearing at the beginning of each regular issue of the PCT Gazette.

METHODS FOR MICROSCALE LASER SHOCK PEENING OF METAL THIN FILMS

SPECIFICATION

CROSS-REFERENCE TO RELATED APPLICATIONS

[0001] This application is based on United States provisional patent application serial no. 60/381,034, filed May 16, 2002, which is incorporated herein by reference for all purposes and from which priority is claimed.

NOTICE OF GOVERNMENT RIGHTS

[0002] The U.S. Government has certain rights in this invention pursuant to the terms of the National Science Foundation award number DMI-98-13453.

BACKGROUND OF THE INVENTION

[0003] Technical Field. The present invention relates to techniques for microscale laser shock peening (LSP), in particular relating to processing of thin metal films.

[0004] Background Art. Shot peening, a process widely known in the art, is a metal treatment process which increases resistance to fatigue and reduces stress corrosion failures, thus preventing premature fatigue failures in metal parts. The shot peening process is accomplished by bombarding the surface of a subject with tiny uniformly sized round steel spheres, to modify the physical characteristics of the target material. Shot peening negates residual surface tensile stress by the introduction of compressive stress, resulting in a compressively stressed surface layer which serves as a deterrent to the outbreak and growth of fatigue cracks, the cause of most material failures.

[0005] However, there are many problems associated with this process. A potentially large target variation prevents execution of the process with a high level of precision. Further, the force of the impact cannot be precisely controlled and can result in damage to the target surface.

[0006] More recently, Laser Shock Processing ("LSP," also known as laser shock peening) has been used as an alternative to shot peening. For example, as described in Clauer et al., "Effects of Laser Induced Shock Waves on Metals," Shock Waves and High Strain Phenomena in Metals-Concepts and Applications, New York, Plenum, pp. 675-702 (1981), a

target to be processed is coated with an opaque, absorptive material, e.g., a special paint or tape that will vaporize when exposed to a pulse of laser energy. A thin layer of translucent material, usually water or glass, is placed on top of the absorptive material. A pulsed laser beam is used to strike the paint or tape, causing some portion of the absorptive material to vaporize. The vapor absorbs the remaining pulsed laser light and is converted into a plasma which is trapped in the gap between the absorptive material and the layer of translucent material. As the heat from the laser is imparted on the trapped plasma, the pressure of the plasma builds to a high pressure and creates a compressive shock wave, part of which is forced into the metal target surface because the pressure is contained by the translucent barrier. That part of the shock wave which is imparted onto the target surface causes plastic deformation of the target surface, causing compressive residual stresses that prevent cracks from growing and thus improving the fatigue life of the target material.

[0007] In Miller et al., "Failure Modes in Surface Micromachined Micro-Electro-Mechanical Actuators," IEEE 98CH36173, 36th Annual International Reliability Physics Symposium, pp.17-25 (1998), and Tanner et al., "MEMS Reliability in a Vibration Environment," IEEE OOCH37059, 38th Annual International Reliability Physics Symposium, pp. 139-145 (2000), failure and reliability problems in micro-electromechanical structures ("MEMS") are discussed. While the dominant material in MEMS is silicon, metal and metallic thin film structures are often indispensable, and metal is a better choice for some applications. Non-metal plates suffer from electrostatic stiction, which has become an common cause of MEMS failure. Metal structures are free from these electrostatic stiction problems, and metal connection lines can be easily integrated into the metal structure. For metallic MEMS structures, it would be advantageous to provide desirable modifications to the physical properties of the metals in order to improve MEMS performance. Accordingly, there exists a need for a process for Microscale LSP which may be used for thin metal films and for MEMS applications.

In addition, LSP processes require extensive modeling for accurate prediction and control of the results. There are several limitations of the LSP models which currently exist in the art. For example, LSP models described by Clauer, et al. and Fabbro et al., "Physical study of laser-produced plasma in confined geometry," J. Appl. Phys., July, 1990, Vol. 68(2), pp. 775-784 (1990), assume that the laser irradiation is uniform and therefore that shock propagation in the confining medium and target is one-dimensional. This assumption is appropriate when the size of a laser beam, whose intensity typically follows a Gaussian

distribution, is relatively large. However, for application to MEMS and metal thin films, a much smaller diameter laser beam must be employed.

[0008] More specifically, the above shock pressure models assume that a certain amount of plasma exists instantaneously once the laser is activated. In reality, laser irradiation first vaporizes the surface layer of the coating, and the vaporized material then quickly evolves into plasma. Water near the plasma outer edge is ionized and becomes strongly absorbent to the incident laser irradiation. At the same time, the absorptive coating is continuously vaporized into the plasma. Explicit consideration of the mass transfer in the LSP system will eliminate the need for prescribing the value of α, the fraction of plasma internal energy used to increase the pressure of plasma, and thus increase the model accuracy, which is crucial for the micro-scale LSP applications. In addition, radial expansion of plasma can no longer be neglected in the micro-scale LSP modeling since it is in the same order of the small beam size. A description of such improved modeling of shock pressure is provided in Zhang et al., "Modeling and Simulation Improvement in Laser Shock Processing," Proc. CALEO'2001, Section A (2001), the contents of which are incorporated fully herein by reference.

[0009] Unfortunately, the effects of finite size and complex geometry on shocking results are neglected in known models in the art. However, these considerations are very important in practice, especially for LSP of small components and LSP near edges of the components. Accordingly, there exists a need for a new modeling technique which is may be used in connection with microscale laser shock processing, and which overcomes the limitations of the prior art models.

[0010] Further still, microscale LSP poses additional challenges in the characterization and measurement of stress/strain fields in shock-treated thin films. Conventional X-ray diffraction methods do not provide the spatial resolution necessary to characterize the residual stress distribution on such a small scale. The spatial resolution of normal X-ray diffraction is typically larger than 0.5mm, which has been used to measure the average stress/strain but is too large to measure the stress/strain distributions in microscale laser shock processing. Accordingly, there exists a need for improved methods for characterization and measurement which can be used in connection with microscale LSP.

[0011] X-ray microdiffraction and instrumented nanoindentation may be used to characterize the stress/strain variations in shock treated thin films with micron spatial resolution. Recent developments in X-ray microdiffraction provide the possibility of measuring the stress/strain fields with micron-level spatial resolution, as described in Noyan et al.,

"Characterization of Substrate / Thin-film Interfaces with X-ray Microdiffraction," Applied Physics Letters, Vol., 72 (25), pp. 3338-3340 (1998), and Wang et al., "Topographic Measurement of Electromigration-induced Stress Gradients in Aluminum Conductor Lines," Applies Physics Letters, Vol. 76 (25), pp. 3726-3728 (2000). The spatial resolution of normal X-ray diffraction is typically larger than 0.5mm, which has been used to measure the average stress/strain but is too large to measure the stress/strain distributions in microscale laser shock processing, as reported in Zhang et al., "Micro Scale Laser Shock Processing of Metallic Components," ASME Journal of Manufacturing Science and Engineering (2000).

[0012] Recent developments in X-ray microdiffraction provide the possibility of measuring the stress/strain fields with micron-level spatial resolution. High brightness X-ray beams are needed for speed and accuracy in X-ray microdiffraction experiments. Otherwise, lengthy sampling times are required to yield meaningful results, and the accuracy can suffer from drifting and noise in such slow and low intensity measurements. For this reason, synchrotron radiation sources are commonly used. The extremely high brightness X-ray beams from synchrotron radiation sources are narrowed down and then focused to micron or sub-micron spot sizes using X-ray optics such as Fresnel Zone Plates (FZP) or tapered glass capillaries, and either white beam or monochromatic X-rays are used.

[0013] In Solak et al., "Measurement of Strain in Al-Cu Interconnected Lines with X-ray Microdiffraction," J. Appl. Phys., Vol. 86(2), pp. 884-890 (1999), the evolution of the stress in aluminum or copper interconnects due to electromigration is reported to have been measured with micron spatial resolution using such techniques. However, the accuracy of the direct stress/strain measurement of the polycrystalline film based on lattice d-spacing variation using Bragg's law has not been well validated. Due to both the divergence and uneven intensity distribution of the incident X-rays, and the insufficient number of grains sampled at each test point, the uncertainty of the Bragg angle may be too large to determine the absolute values of the lattice d-spacing, as discussed in Noyan et al., "Divergence Effects in Monochromatic X-ray Microdiffraction Using Tapered Capillary Optics," Review of Science Instruments, Vol. 71(25), pp. 1991-2000 (2000). On the other hand, Noyan et al., "Characterization of Substrate / Thin-film Interfaces with X-ray Microdiffraction," Applied Physics Letters, Vol., 72(25), pp. 3338-3340 (1998) and Noyan et al., "Deformation Field in Single-crystal Semiconductor Substrates Caused by Metallization Features," Applied Physics Letters, Vol. 74(16), pp. 2352-2354 (1999), report that relative stress/strain variations can be reliably measured with micron-level spatial

resolution by recording the diffraction intensity contrast of the underlying single crystal silicon substrate

[0014] Accordingly, there exists a need for techniques for processing, modeling and characterization which may be used in conjunction with LSP processing of thin metal films.

SUMMARY OF THE INVENTION

[0015] An object of the present invention to fulfill needs in the field of laser shock peening by providing a method for laser shock peening of metal thin films with micron spatial resolution.

[0016] It is a further object of the present invention to provide techniques for modeling a microscale LSP process.

[0017] It is a further object of the present invention to provide techniques for characterization of a microscale laser shock-treated sample.

[0018] It is a further object of the present invention to provide microscale LSP processing, modeling, and characterization techniques which may be utilized to improve the reliability of MEMS systems.

[0019] In order to meet these and other objects of the present invention which will become apparent with reference to further disclosure set forth below, the present invention provides a technique for microscale laser shock processing. One exemplary method for laser shock processing of metal thin films comprises the steps of providing an absorptive coating on a target metal thin film on a layered structure, providing a translucent barrier layer on top of the absorptive coating, and applying a laser to an area of the target material such that the absorptive material is vaporized to form a high pressure plasma which imparts a shockwave on the target metal thin film. Further embodiments of the present invention include utilization of this process in a scheme for MEMS manufacturing.

[0020] The present invention further provides a method for modeling a microscale laser shock process, which includes the steps of considering the spatial profile of a laser beam, considering the radial expansion of plasma, determining a value for plasma energy which is related to the laser beam intensity, and furthermore considering the plasma energy expended by the breakdown of the target material. A further embodiment of this inventive modeling method may also include consideration of the plasma energy expended via the breakdown of the translucent barrier layer, where that layer is comprised of water.

[0021] The present invention further provides a method for measurement and characterization of the stress and/or strain field of microscale laser shock treated metals. An exemplary embodiment of this method includes the steps of determining the curvature of a metal thin film before laser shock peening, determining the curvature of the metal thin film after laser shock peening, and finally determining at least one of the average stress and average strain based on the determined difference in curvature between the measurements before laser shock peening and after laser shock peening.

[0022] The present invention provides another method for measurement and characterization of the stress and/or strain field of microscale laser shock treated metals. An exemplary embodiment of this method includes the steps of monitoring the surface integrity of the target metal thin film using fluorescence measurement, determining a suitable X-ray beam energy level for penetration of the target metal thin film which is greater than the K absorption edge of the material, employing an X-ray beam to penetrate the top layer of the target metal thin film, focusing the incident X-ray beam using a tapered glass capillary to form a microbeam directed on a spot on the target metal thin film, calibrating the position of the shocked region relative to the X-ray microbeam, scanning the sample relative to the microbeam and recording the diffraction intensity of the single crystal substrate at one or more locations on the target metal thin film using a scintillation detector in a symmetric reflection configuration, identifying deformations in the substrate of the target metal thin film using X-ray diffraction intensity contrast data, and determining strain or stress components based on the X-ray diffraction intensity contrast data.

[0023] The present invention provides another method for measurement and characterization of the stress and/or strain field of microscale laser shock treated metals. An exemplary embodiment of this method includes the steps of determining the hardness of a surface of a shock-treated metal thin film at a plurality of points using instrumented nanoindentation, plotting one or more curves of the determined hardness at a plurality of points, and determining the residual stress based on the plotted curves.

[0024] The accompanying drawings, which are incorporated and constitute part of this disclosure, illustrate preferred embodiments of the invention and serve to explain the principles of the invention.

BRIEF DESCRIPTION OF THE DRAWINGS

[0025] Fig. 1 is an illustrative diagram showing a laser shock process in accordance with the present invention;

[0026] Fig. 2 is an illustrative diagram showing the various layers in laser shock processing as may be used in modeling an LSP process;

[0027] Fig. 3 is a graph showing mass flow from water into plasma and normalized laser intensity presented in accordance with an exemplary embodiment of the present invention for modeling an LSP process;

[0028] Fig. 4 is a graph which compares the shock pressure results of a modeling method in accordance with an exemplary embodiment of the present invention and other modeling methods;

[0029] Fig. 5 is a graph which illustrates the benefits of considering the radial and axial expansion of plasma in an exemplary embodiment of the LSP process modeling method of the present invention;

[0030] Fig. 6 is an illustrative diagram showing data obtained using the wafer curvature method in accordance with an exemplary embodiment of the present invention for characterizing stress and strain fields for LSP-treated samples;

[0031] Fig. 7 is a graph showing data obtained using the wafer curvature method in accordance with an exemplary embodiment of the present invention for characterizing stress and strain fields for LSP-treated samples, as shown in graphical form;

[0032] Fig. 8A is a graph of fluorescence measurements of copper thin films using X-ray energy showing the fluorescence spectra of copper thin films, as such measurements may be used in accordance with an exemplary embodiment of the present invention for characterizing stress and strain fields of LSP-treated samples;

[0033] Fig. 8B is a graph of fluorescence measurements of copper thin films using X-ray energy showing the fluorescence intensity distribution measured across a copper thin film surface, as such measurements may be used in accordance with an exemplary embodiment of the present invention for characterizing stress and strain fields of LSP-treated samples;

[0034] Fig. 9 is an illustrative graph showing the variation of diffraction intensity contrast with laser pulse energy, as such data may be used in accordance with an exemplary embodiment of the present invention for characterizing stress and strain fields of LSP-treated samples;

[0035] Fig. 10 is a graph of simulation results of the strain energy density located at the copper-silicon interface, illustrating principles in accordance with an exemplary embodiment of the present invention for characterizing stress and strain fields of LSP-treated samples;

[0036] Figs. 11A-C are graphs which compare strain energy density and X-ray diffraction intensity contrast for samples of various properties, as determined using characterization methods in accordance with the present invention;

[0037] Figs. 12A-B are graphs showing loading and unloading curves at different locations, as associated with exemplary characterization methods in accordance with the present invention for determining stress and/or strain using an instrumented nanoindentation technique.

[0038] Throughout the Figs., the same reference numerals and characters, unless otherwise stated, are used to denote like features, elements, components or portions of the illustrated embodiments. Moreover, while the present invention will now be described in detail with reference to the Figs., it is done so in connection with the illustrative embodiments.

DETAILED DESCRIPTION OF THE PREFERRED EMBODIMENTS

[0039] Referring to Fig. 1, an exemplary process for LSP according to the present invention is shown. A coating material 12 is applied on target metal thin film 13. In one embodiment of the present invention, copper films of lμm and 3μm on 1-inch round single crystal silicon wafers with (001) orientation and 0.254 mm thickness may be treated using LSP. Coating material 12 may be one of several different materials such as organic paint, tape or thin metallic foil. A translucent material 11 is provided on top of coating material 12, and is generally either a clear liquid or glass. Laser beam 10 is focused on a portion of target metal thin film 13, and a short and intense laser pulse is irradiated whereby a plasma is formed as coating material 12 is vaporized by the heat from laser beam 10.

[0040] In one embodiment of the present invention, a Q-switched Nd:YAG laser with pulse duration of 50 ns and wavelength of 355 nm and intensity of greater than 1 GW/cm^2 is used. The laser beam size should be less than 1 millimeter. The plasma 14 is continually heated by laser beam 10 until the high temperature, high pressure plasma causes a shockwave to be imparted from the plasma 14. The shockwave penetrates into target metal thin film 13 and causes desirable effects on the shocked portion of target metal thin film 13. Additionally, during laser shock processing, the sample may be covered with an aluminum foil with a very thin layer of vacuum grease in between. Thus, thermal effects are isolated and only shock effects are experienced by the sample. An aluminum foil of 16 μm thickness is used.

[0041] Referring to Fig. 2, the layers of material of the LSP process of the present invention are shown. A top layer is an unshocked water layer 21. A next layer below unshocked water layer 21 is shocked water layer 22. Next, plasma layer 23 defines the region in which a plasma is generated from laser beam heat during LSP processing. Coating layer 24 and shocked metal layer 25 are contained within the region from which the generated shockwave originates and propagates. A bottom region, unshocked metal thin film 26, describes the lower portion of the metal thin film which remains substantially unaffected as a result of the LSP process.

[0042] The LSP process of the present invention for use with thin metal films may be used to improve performance characteristics for MEMS such as gears, switches, etc. In one exemplary LSP process for metal thin films according to the present invention, the raw material which is used to create the MEMS structures may be shocked first, and then the MEMS structures may be etched from the shocked bulk raw material. In another exemplary embodiment, the MEMS structures may first be etched, and then shocked according to the LSP process of the present invention. Additionally, the LSP process according to the present invention is process environment compatible, and therefore is compatible with the MEMS production process and may be easily integrated into the MEMS manufacturing process.

[0043] In an exemplary embodiment according to the present invention, a method for modeling LSP processes for metal thin films is provided. Under typical conditions of LSP, the speed of plasma expansion is lower than the shock speed, and thus the shock wave precedes plasma expansion. This resembles the case of a laser supported combustion ("LSC") wave. LSC waves in air and in a vacuum are extended in accordance with an exemplary embodiment of the present invention for LSP modeling.

[0044] In laser shock peening, water is converted into plasma due to plasma and laser induced water breakdown. At the same time, the coating is continuously vaporized and converted into plasma. Mass, momentum and energy are conserved across the shock wave. To model the process, the following assumptions may be made: (1) plasma expands only in the axial direction in the early stage; density, internal energy and pressure of the plasma are uniform within the plasma volume but can vary with time; (2) plasma obeys ideal gas laws; (3) only the coating layer is vaporized, the metal target experiences negligible thermal effects; and (4) the coating layer is thin and well coupled with the metal target, thus the shock pressure and the particle velocities of the coating layer and the metal target are equal.

[0045] For convenience, the water-plasma-target system may be divided into six regions for modeling purposes, as discussed above with respect to Fig. 2. Subscripts *w* denote water, *m* metal, *c* the coating layer, *p* plasma, *L* the side of plasma near water, *R* the side of plasma near solid, and *0* the property of an unshocked region. *D* is the shock velocity, *U* the particle velocity, *E* the internal energy, ρ the density, and *P* the pressure. Unshocked properties are taken as known values, with the purpose of the model to accurately determine the shocked properties. In accordance with these principles, the shocked and unshocked properties of water are related by mass, momentum, and energy conservation, and shock speed constitutive relations as follows:

$$\rho_{w0} / \rho_w = 1-(U_w - U_{w0}) / (D_w - U_{w0}) \quad (1)$$

$$P_w - P_{w0} = \rho_0 \, (D_w - U_{w0})(U_w - U_{w0}) \quad (2)$$

$$(E_w + U_w^2/2) - (E_{w0} + U_{w0}^2/2) = \frac{1}{2}(P_w + P_{w0})(\frac{1}{\rho_{w0}} - \frac{1}{\rho_w}) \quad (3)$$

$$D_w = D_{w0} + S_w U_w \quad (4)$$

[0046] For water, $U_{w0} = 0$ m/s, $P_{w0} = 10^5$ Pa, $E_{w0} = 0$ J/kg, $\rho_{w0} = 997.9$ kg/m^3, $D_{w0} =$ 2,393 m/s, and $S_w = 1.333$. S_w is a coefficient relating shock speed D_w to U_w, the particle velocity and D_{w0}, the shock speed at infinitesimally small particle velocity. Substituting subscript *m* for *w* in Eqs. 1-4, four more equations between shocked and unshocked properties of metals may be obtained. $U_{m0} = 0$ m/s, $P_{m0} = 10^5$ Pa, $E_{m0} = 0$ J/kg. For copper, $\rho_{m0} = 8{,}939$ kg/m^3, $D_{m0} = 3{,}933$ m/s, and $S_m = 1.489$. Mass and momentum conservation at the interfaces of water-plasma-metal at any instant requires:

$$\rho_w (U_{pL} - U_w) = \rho_p \, U_{pL} \quad (5)$$

$$\rho_c (U_{pR} - U_c) = \rho_c \, Vrec = \rho_p U_{pR} \quad (6)$$

$$\rho_p + \rho_p U_{pR} U_c = \rho_c \quad (7)$$

$$\rho_p + \rho_p U_{pR} U_w = \rho_w \quad (8)$$

[0047] The current mass of the plasma is equal to the integration of the mass flows into plasma. The mass conservation of plasma requires:

$$\rho_P(t) \int_0^t (U_{PL} + U_{PR}) dt = \int_0^t (MF_w + MF_c) \, dt \quad (9)$$

where MF_w is the mass flow from water into plasma, and MF_c the mass flow from the coating into plasma. The energy conservation of plasma considers the absorption of incident

laser irradiation, E_{pt} the total energy stored in the plasma, W_p the work done by the plasma, and E_{MF} the energy exchanges through mass flow. The total energy of plasma consists of kinetic energy and internal energy, and using the ideal gas law, the internal energy of plasma is related to its density, specific heat ratio γ (about 1.3), and pressure. If AP is the fraction of laser energy absorbed by plasma, and $I(t)$ the laser intensity, the energy conservation of plasma requires:

$$E_{pt} + W_p - E_{MF} = \int_0^t AP \times I(t)dt \tag{10}$$

[0048] AP can be decided from experiments. Therefore, the equations of this 1D shock pressure model are closed and all the variables involved can be solved as a function of time. Radial expansion of plasma is a more significant concern in micro-scale LSP than in mm-scale LSP because such expansion may not be neglected due to the small beam size. Once plasma is created, radial expansion of plasma commences. A rarefaction wave propagates into the plasma from the edge at the sound speed of the plasma. After a characteristic time $T_r = R_0/a$, where R_0 is the radius of the laser beam and a is the sound speed of the plasma, the rarefaction wave coalesces at the center of the spot. The pressure of the plasma drops and deviates from the 1D values afterwards. Axial relaxation starts after the laser pulse terminates, thus the characteristic time for axial expansion is $T_z = T_p$, where T_p is pulse duration. The temporal evolution of the plasma depends on the values of T_r and T_z. For a laser used in this exemplary embodiment of the present invention, $R_0 = 6$ microns, $T_z = T_p = 50$ ns, and sound speed of plasma $a = 300$ m/s, $T_r = 20$ ns, thus radial relaxation occurs earlier than axial relaxation. The following power scaling laws which are known in the art may be applied:

$$\begin{aligned}
&t < T_r && P = P_{1D} \\
& && R = R_0 \\
&T_z > t < T_r && P = P_{1D}(t/T_r)^{-4/5} \\
& && R = R_0(t/T_r)^{1/2} \\
&t < T_z && P = P_{1D}(T_r/T_z)^{4/5}(T_z/t)^{6/5} \\
& && R = R_0(T_z/T_r)^{1/2}(T_z/t)^{-4/5}
\end{aligned} \tag{11}$$

where P_{1D} is the plasma pressure from 1D model described above.

[0049] In accordance with the method for modeling of the present invention, in order to improve the accuracy of the modeling technique for laser shock peening on micron scale, the spatial profile of the laser beam may also be considered. Shock pressure obeys Gaussian spatial

distribution, but with its $1/e^2$ radius equals to $\sqrt{2R(t)}$, where $R(t)$ is the radius of plasma in Eq. 11. Let r be the radial distance from the center of the laser beam, the spatially uniform shock pressure $P(t)$ relates to the spatially non-uniform shock pressure as

$$P(r,t) = P(t)\exp(\frac{r^2}{2R^2(t)}) \tag{12}$$

[0050] The evolution of mass flow from water into plasma is shown in Fig. 3, which also shows the laser intensity profile 31 normalized to the peak intensity. The mass flow 32 peaks after laser intensity peaks. The reason is that even after the laser intensity peaks, the plasma irradiation sustains the mass flow for a period of time. As laser intensity increases, plasma accumulates more energy to irradiate. Accordingly, it takes longer for the mass flow to peak when laser intensity increases. The mass flow from the coating layer into plasma has similar features. The mass flows contribute to the evolution of plasma and the expansion of plasma imparts high shock pressures into water and target solid.

[0051] Fig. 4 compares the 1D shock pressure determined using a model in accordance with an exemplary embodiment of the present invention, and a present model of Zhang et al. Graph 40 illustrates the difference between results of the previous model 41 and the results generated by a model in accordance with the present invention 42. The previous model assumes that a constant fraction $\alpha = 0.2$ of plasma energy is used to increase the shock pressure. In the model according to the present invention, such conversion is inherently considered in the energy balance relations. As shown, the prior art model determined a higher peak pressure at laser intensity of 2 GW/cm^2, a comparable value at 4 GW/cm^2, and a lower value at 6 GW/cm^2 than the current model. This is indicative of the shortcoming of using a constant value of α for different laser intensities in the previous model. The pressures recover to zero values faster in the current model than in the previous model. The reason is that in the current model, plasma energy is used for the breakdown of water and target material besides the expansion of plasma, while in the previous model only the 1D expansion of plasma was considered.

[0052] The increased accuracy of the 2-D model of the present invention is illustrated in Fig. 5 by graph 50. The temporal evolution of shock pressure and the radius of plasma at laser intensity of 4 GW/cm^2 are shown. Data line 51 represents the shock pressure of the 1-D models of the prior art. Data line 52 represents the shock pressure of a model according to an exemplary embodiment of the present invention. Data line 53 represents shock pressure according to another exemplary embodiment of the present invention, taking into account the

multi-dimensional radial and axial expansion effects of the plasma. A non-linear increase of plasma radius occurs after 20ns. The shock pressure deviates from the 1D results after the rarefaction wave merges at the beam center according to the power laws in Eq. 11.

[0053] Microscale LSP poses challenges in the characterization of the stress/strain fields in thin films. Conventional X-ray diffraction does not provide the spatial resolution necessary to characterize the residual stress distribution. The present invention addresses these issues and provides several methods for characterization of laser shock-treated thin film samples.

[0054] In an exemplary embodiment of the present invention for determining average stress/strain values for LSP-treated metal thin films, a wafer curvature method is employed. Curvature measurements may be performed to determine whether microscale LSP has induced compressive residual stress in metal thin films. The curvatures of the wafers before coating, and after coating with and without laser shock processing may be measured using an optical profiler (Wyko 3300). The average residual stress in the thin films on the silicon substrates can be computed according to Segmüller et al., "Automatic X-ray Diffraction Measurement of the Lattice Curvature of Substrate Wafers for the Determination of Linear Strain Patterns," J Appl., Phys., Vol. 51(12), pp. 6224-6230 (1980), the contents of which are incorporated herein:

$$\sigma f = \frac{M_s t_s^2}{6 t_f}(1/R - 1/R_0) \tag{13}$$

where t_s and t_f are the thickness of the substrate and the film, respectively, R and R_0 the current and original wafer radius (seen from the film side), respectively, and M_s the biaxial modulus of the substrate. For the (001) single crystal silicon wafer, M_s = 180.5GPa. Eq. (13) applies under the assumption of small deformation and pure elastic bending of a thin plate. Furthermore, it is assumed that the residual stress is uniform within the whole depth of the film.

[0055] Referring to Fig. 6, the 2D contours of a 1μm shock-treated sample is shown in graph 60 as measured with an optical profiler. Curvature of the wafer can be measured from the profiles, as shown in Fig. 7. The results of the measurement of a target sample before LSP with no coating, before LSP with coating, and with coating after LSP are compared. Copper has a larger expansion coefficient than silicon. After coating and cooling down, the copper film contracts more than the silicon substrate. Thus, the copper film experiences tensile stress. The substrate close to the film experiences compressive stress due to a balance of force. As a result, the initially convex curvature of the wafer becomes less convex when the film stress is tensile. On the other hand, when the film stress is compressive, the wafer surface will become more convex. This explains the profile changes in Fig. 7.

[0056] The film stress after coating increases with the increase in film thickness. Tensile stress tends to make the wafer more concave. Using Eq. (1), the residual stress variations in the thin films may be computed. Shock-treated samples exhibit tensile residual stresses after coating, and both change to compressive after laser shock processing. The curvature measurement may be used to estimate the average stress in the thin film. To study the local distribution of the stress/strain field, however, other techniques may be employed, as are discussed hereinafter in other embodiments in accordance with the present invention.

In another exemplary embodiment of the present invention, a diffraction intensity contrast method is used to characterize shock-treated samples. An X-ray microbeam is used to penetrate the top thin film layer (which may be composed of, for example, polycrystalline) and the diffraction intensity of the single crystal substrate is recorded. The stress/strain in the thin film is coupled to and deforms the substrate. The transition from perfect to imperfect crystal results in an increase in the diffraction intensity, because the intensity of X-ray diffraction is proportional to the square of the structure factor F of the material:

$$F_{hkl} = \sum_{1}^{N} f_n e^{2\pi i(hu_n + kv_n + lw_n)} \tag{14}$$

where f_n is the atomic scattering factor, h, k and l are the Miller indices of the lattice planes, and u_n, v_n and w_n are the locations of the atoms in the unit cell of the lattice.

[0057] For a diffraction to be present, the diffraction angle must satisfy Bragg's law,

$$\lambda = 2d\sin(\theta) \tag{15}$$

where d is the lattice spacing, θ the diffraction angle, and λ the wavelength of the incident X-rays. At the same time, the structure factor must be non-zero. For a perfect crystal, the lattice planes are parallel, the angle width of strong diffraction is very narrow, and some of the lattice planes have a zero structure factor. For an imperfect crystal, however, the crystal is made up of small mosaic blocks or sub-grains, the blocks are disoriented so that they are essentially nonparallel, and some of the extinction diffractions of the ideal crystal become non-zero. Laser shock peening induces local stress/strain in the single crystal substrate. The strained region induces mosaic structures, while the strain-free region is close to perfect crystal. Due to the increased bandwidth of strong diffraction and the reduced extinction processes, the integrated X-ray diffraction intensity increases in the locally strained region compared with the strain-free region. A single crystal substrate is best used in accordance with this method, and the film layer should generally be thin enough to get strong diffraction signals.

[0058] Discussing this exemplary embodiment in further detail, focusing lenses for visible light use materials with index of refraction substantially larger than t. The index of refraction n for most materials at X-ray wavelength is:

$$n = 1 - \delta + i\beta \tag{16}$$

where δ is a small number less than 1, and, β is the complex part of the refraction index. The real part of the refraction index is less than 1. Thus, lenses for visible light cannot be used to focus X-rays. Only optics based on diffraction and interference (multilayer mirrors and zone plates, etc.), or on total external reflection can be used for the focusing of X-rays.

[0059] For visible light, when the light beam propagates from a higher index medium towards a lower index medium with an incident angle larger than the critical angle, total reflection occurs and the reflected light stays in the high-index medium (termed total internal reflection). For X-ray, total reflection occurs when the grazing angle on the surface of an optical medium, such as glass or metal, is less than the critical angle. The reflected X-ray is outside the optical medium.

[0060] The critical angle θ_c for total external reflection, as described in Erko, is:

$$\theta_c = \sqrt{2\delta} \tag{17}$$

where δ has the same meaning as in Eq. (16). For the lead glass capillary used in this exemplary embodiment of the present invention, the incident bore diameter may be approximately 50 μm, the exit bore diameter approximately 5μm, and the length approximately 8cm. The tapered capillary tube may be parabolic in shape. This tube is aligned to receive the X-ray beam from the synchrotron beamline, and successively focus the beam to a small spot size by total external reflection. At the same time, the gain of the capillary system, defined as the intensity at the exit of the capillary to the intensity at entrance, may be higher than 40. Both small spot size and increased intensity are desirable in X-ray microdiffraction.

[0061] To use the diffraction contrast method of characterization in accordance with an exemplary embodiment of the present invention, a suitable X-ray energy level should be used and the film thickness should not be too high. It is thus necessary to determine the decay of the incident X-ray beam in the film. The absorption of an incident X-ray by a thin film is:

$$I / I_0 = \exp(-\mu z / \sin(\theta)) \tag{18}$$

where I_0 is the incident X-ray intensity, I the intensity reaching the silicon substrate, z the thickness of the film, μ the linear absorption coefficient of the film, and θ the diffraction

angle. For copper, μ=405.6cm^{-1} at 8.SKeV, and 2411.8 cm^{-1} at 9.1KeV. The diffraction signal from the silicon substrate experiences a second decay before it is detected. In an exemplary embodiment of the present invention, the total decay for samples with different film thicknesses may be as shown in Table I below:

Table I

X-ray type	Film thickness (micron)	$\mathrm{Exp}(-2\mu z/\sin(\theta))$
8.5KeV $\mu = 405.6cm^{-1}$	1	0.8599
	1.5	0.7973
	3	0.6358
9.1KeV $\mu = 2411.8cm^{-1}$	1	0.4075
	1.5	0.2601
	3	0.0677

[0062] X-ray energy of 8.5KeV may be used in accordance with the present invention because copper film is less absorbent of the incident X-ray so that the substrate diffraction signal can be strong. The energy level of 8.5 KeV may beneficially be chosen to be lower than the critical energy W_k that can excite the $K\alpha$ fluorescence radiation of the copper thin film. To excite the fluorescence radiation efficiently, the X-ray energy should be larger than and close to the K absorption edge of the material:

$$E > W_k = hc/\lambda_k \qquad (19)$$

where E is the incident X-ray energy and λ_k is the wavelength of the K absorption edge. In the exemplary embodiment of the present invention, the K absorption edge of copper is determined to be 8.98KeV, thus, 9.1KeV would be a good choice for detecting the fluorescence of copper.

[0063] In this exemplary embodiment of a method for x-ray microdiffraction, IBM's X20A beamline of the National Synchrotron Light Source at Brookhaven National Laboratory is used, however those skilled in the art will understand that this light source may be replaced with others in the scope of the present invention. First, fluorescence tests may be carried out using a 9.1KeV beam energy to monitor the surface integrity of the sample. Next, monochromatic X-rays at 8.5 KeV ($\lambda = 1.459$ angstroms) may be used in the diffraction tests. The incident X-ray beams are focused using a tapered glass capillary to form a 10 micron x 10 micron spot on the sample surface. Si (004) diffraction from the substrate is collected using a scintillation detector in a symmetric reflection configuration at $2\theta \cong 65°$. The thin film sample is vacuum held onto

a motorized, high precision XYZ stage. Next, the position of the shocked region relative to the X-ray beam is calibrated. Then, by scanning the sample relative to the beam (in 2 or 4 microns spacing, in this exemplary embodiment of the present invention), the distribution of the Si(004) intensity across the shocked region may be recorded.

[0064] In the diffraction test of an exemplary embodiment of the present invention, the 2θ angle that has maximum intensity of Si(004) diffraction is found by rocking the sample to satisfy Bragg's law as in normal X-ray diffraction. After the optimum 2θ angle is found, it is fixed in the following diffraction tests. The shock-treated sample is scanned relative to the X-ray beam, and the diffraction signal at that fixed angle is sampled for a certain period of time.

[0065] The major purpose of the fluorescence measurement in this test is to monitor the surface integrity of the films. Referring to Fig. 8A, graph 80 shows the X-ray fluorescence spectra of copper films of different thicknesses. The peaks of the three films have the same locations, and the fluorescence intensity increases with the increase in the film thickness. The location of the peak in the fluorescence spectra is a property of the material itself. As an example, for copper, the fluorescence $K\alpha_1$ energy is 8.04778KeV, coincident with the large peaks. The small peaks have energy of 9.1KeV, which is the same as that of the incident X-ray beam. This peak comes from the reflection of the incident beam. The fluorescence intensity increases with the volume of material sampled by the X-ray beam. X-rays at 9.1KeV sample the whole thickness of the film, and the thicker the film, the stronger the fluorescence intensity.

[0066] In an exemplary embodiment of the present invention, as shown in Fig. 8B, the X-ray beam scans across the film surface in 2-micron spacing, and the integrated intensity of the fluorescence spectra at each point is recorded as shown the graph 81. Note that the spacing of the recorded data points may be modified in the scope of the present invention. The variation of the integrated intensity reflects the mass variation in the film. As shown, the averages of the intensity are all horizontal, and the standard deviation is small, indicating good uniformity of the films.

[0067] Referring to Fig. 9, the peak values of diffraction intensity contrast under various conditions are compared in graph 90. For the same film thickness, with the increase of pulse energy, the diffraction contrast increases, and a trend of leveling off at high laser pulse energy can be seen in all three curves. Under the same level of laser pulse energy, thicker films result in higher contrast of diffraction intensity. Thicker films have longer time to absorb the shock energy than thinner films, and under the same level laser pulse energy, the stress/strain fields at

the interface are stronger in thicker films than in thinner films, as demonstrated through simulations results (shown in Fig. 10, graph 100).

[0068] The location of stress/strain concentration and relative change of stress/strain in metal thin film can be inferred from the diffraction contrast of the substrate (See, e.g., Noyan et al.; Wang et al.). It has also been shown by Cullity that the diffracted intensity varies monotonically and non-linearly with the "bending strain," but the quantitative correspondence between local stress/strain and the increase in diffraction intensity is a complex problem and is still under investigation.

[0069] Strain or stress components can be correlated directly with the X-ray diffraction intensity contrast. Referring back to the origination of the X-ray diffraction intensity contrast, the increase of diffraction intensity comes from the increased mosaic structure in the substrate induced by the stress/strain field in the thin film at the interface. An index evaluating this combined effect is strain energy density D which is defined as:

$$D = \frac{1}{2}\varepsilon_{ij}\sigma_{ij} = \frac{1}{2}(\varepsilon_{11}\sigma_{11} + \varepsilon_{22}\sigma_{22} + \varepsilon_{33}\sigma_{33} + \varepsilon_{12}\sigma_{12} + \varepsilon_{13}\sigma_{13} + \varepsilon_{23}\sigma_{23}) \qquad (20)$$

where ε_{ij} is the total strain (elastic plus plastic) tensor and σ_{ij} the residual stress tensor. The unit of D is J/m^3.

[0070] Strain energy density is difficult to measure experimentally, but its value can be extracted from simulation. Simulation shows that the strain energy density is higher for higher pulse energies and greater film thicknesses. Similar trends are observed in Fig. 9.

[0071] Profiles of X-ray diffraction intensity contrast of single line shock processed 1μm and 3μm samples are compared with the profiles of strain energy density in charts 110 and 111 of Fig. 11A and 11B, respectively. The profiles from simulation and from X-ray experiment come into good agreement when the Y-axes are properly adjusted. For the single line shocked case, both 1 μm and 3 μm samples show a single central peak. For the shocked 7-lines case of the 1 μm sample, however, both the intensity contrast in the X-ray experiment and the strain energy density in simulation show a rising saddle peak (chart 112, Fig. 11C). Stress/strain is relatively uniform within the directly shocked region in the case of 7-lines, but the transition from a uniformly shocked region to a shock free region results in stress concentration. Strain energy density increases in these transitional regions, which is the cause of the saddle shape in chart 112.

[0072] The fact that peak location and peak shape show good agreement simultaneously indicates that the two quantities may be linearly related. Let *XDC* be the X-ray diffraction intensity contrast. From the figures and discussion, an empirical relation may be inferred:

$$D \approx K(XDC-1) = \frac{\max(D)}{\max(XDC-1)}(XDC-1) \tag{21}$$

[0073] Under the condition of equi-biaxial stress distribution, Eq. (21) reduces to:

$$\varepsilon_{11}\sigma_{11} = \varepsilon_{22}\sigma_{22} \approx K(XDC-1) \tag{22}$$

where K is a proportional coefficient. This linear correlation is relatively well obeyed for other conditions as well. The linear correlation between strain energy density and X-ray microdiffraction contrast makes it possible to determine the strain field gradient directly from the measurement of X-ray diffraction intensity contrast.

[0074] In yet another exemplary embodiment of a method for characterization of shock-treated metal thin films in accordance with the present invention, an instrumented nanoindentation method is used.

[0075] Nanoindentation is a destructive method, it can only detect the stress/strain field already changed from the original state, and it is also very sensitive to environmental disturbances and local surface quality variations of the sample, such as defects and grain boundaries. All these factors lead to relatively large scattering in the testing data. Despite the scattering, the increase in hardness and the presence of local compressive residual stress in the shocked region may be detected through this method, and the general trends in nanoindentation tests agree with the trends in simulation and X-ray microdiffraction.

[0076] Instrumented nanoindentation may be used to provide high spatial resolution in testing hardness of shock-treated samples. Instrumented nanoindentation provides a continuous record of the variation of indentation load, P, as a function of the depth of penetration, h, into the indented specimen. Comprehensive theoretical and numerical studies have been carried out to elucidate the contact mechanics and deformation mechanism in order to systematically extract material properties from the P versus h curves. The P-h curves have been used to obtain many material properties, such as hardness, Young's modulus, yield strength, and work hardening exponent. Of special interest is that instrumented nanoindentation can be used to estimate the sign and magnitude of the stress/strain field in thin films.

[0077] The numerical simulations in the prior art assume that the indentation is a frictionless, quasi-static indentation of an isotropic elasto-plastic substrate by an elastic indenter, and the indented substrate is permitted to undergo isotropic strain hardening. This assumption is

reasonable for nanoindentation of ductile metals using diamond Berckovich indenters. The analysis is valid within the continuum mechanics regime, and this requires that the indented area covers at least five grains of the substrate material. It is also assumed that the residual stress in the sample is or is close to equi-biaxial, i.e., $\sigma_x = \sigma_y$, and the stress should be uniform within a depth of at least 3 times the width of the indenter contact radius.

[0078] If there are pre-existing residual stress and/or pre-existing plastic strains, the indentation of the specimen will be influenced by the stress/strain field. The equi-biaxial tensile stress in a film is equivalent to the combination of a hydrostatic tensile stress plus a differential compressive stress in the depth direction. This differential compressive stress is in the same direction as indentation. Thus, tensile residual stress aids indentation by increasing the contact area for a given indentation load or by lowering the indentation load needed to penetrate the material to a certain depth. On the other hand, the equi-biaxial compressive residual stress in the film is equivalent to the combination of a hydrostatic compressive stress plus an in-depth direction tensile stress. This differential tensile stress is in opposite direction of the indentation and tends to impede indentation. Thus, the method of instrumented nanoindentation can be used to determine the sign and estimate the magnitude of the stress/strain field in shock treated thin films in addition to hardness.

[0079] In an exemplary embodiment of the instrumented nanoindentation characterization method of the present invention, shock treated 1 μm samples may be tested using a Triboscope Nanomechanical Test System from Hysitron Inc. The loading/unloading curves are recorded digitally. The system calculates the value of hardness P_{ave} (= maximum load / true contact area) directly, with the noises in measurement accounted for. Based on repeated measurements, the Young's modulus of the copper thin film in this study uses a fixed value, E_f=126GPa. The Poisson ratio is ν_f=0.38, taken from bulk material. The Young's modulus and Poisson ratio of the diamond Berkovich nanoindenter used are: E_i =1140GPa and ν_i =0.0707. The included angle of the Berkovich indenter tip in this exemplary embodiment is 24.7°. The effective Young's modulus of the indenter-specimen system is defined as:

$$E^* = 1/\left(\frac{1-\nu_f^2}{E_f} + \frac{1-\nu_i^2}{E_i}\right) \tag{23}$$

[0080] Thus, E^* =130.49GPa. In all of the measurements the maximum load is fixed at $1000\,\mu N$, and the loading and unloading rates are both $100\,\mu N/s$. The shocked region is scanned perpendicular to the centerline, with the spacing between neighboring points at 12.7 microns.

[0081] Compared with the shock free region and despite the scattering in the data, the trend of increase in hardness in the shock treated region is apparent. The increase of hardness arises from two causes: one is work hardening due to plastic deformation (in a narrow central region only) and the other is the compressive residual stress in the shock treated region. The range of obvious hardness increase is about 150 microns on each side from the center. This range is larger than that in X-ray diffraction and simulation.

[0082] The sign of the stress, which cannot be determined using the X-ray microdiffraction method described herein, can be determined by studying the loading/unloading curves in instrumented nanoindentation. The loading and unloading curves at representative locations of the shock treated region are shown in Figs. 12A and 12B on charts 120 and 121, for pulse energy of 244μJ and 209μJ, respectively. From these curves, the signs of the residual stresses can be determined. The reference curve (the dashed line) represents measurements taken at regions distant from the shocked region. Compared with the reference curve, the loading curves close to the center of the shocked region rise up for both energy levels, indicating that to reach the same penetration depth, a larger load is needed. This implies compressive residual stress in the shock treated region. The sign of the stress can be determined from the curve - when the curve is more rigid than the reference curve, i.e., larger load for same deformation, the local area of the film is harder and is in relative compressive stress to the reference area, which is assumed to have negligible residual stress.

[0083] All of the methods described herein may be used to improve the manufacturing process for MEMS. Some metal microstructures, such as micro-electromechanical actuators, metal gears, and metal switches, experience cyclic loads in service. Wear resistance and fatigue performance of these metal structures should be improved to increase the reliability of the system. Microscale LSP can induce favorable residual stress distributions in bulk metal targets with micron-level spatial resolution. It may potentially be used to improve the wear resistance and fatigue performance of metal film structures. The most popular metallic MEMS materials are copper, nickel and aluminum. Microscale LSP will not bring adverse effects to these micro-devices, since thermal effects are negligible and the water curtain will carry away possible contamination of vaporized materials, and water does not have compatibility problems with MEMS materials and structures. Accordingly, one skilled in the art will understand that the present invention may be utilized to improve the manufacturing and performance of MEMS.

[0084] The foregoing merely illustrates the principles of the invention. Various modifications and alterations to the described embodiments will be apparent to those skilled in

the art in view of the teachings herein. It will thus be appreciated that those skilled in the art will be able to devise numerous systems and methods which, although not explicitly shown or described herein, embody the principles of the invention and are thus within the spirit and scope of the invention.

CLAIMS

1. A method for processing metal thin films, comprising the steps of:

(a) providing an absorptive coating on a target metal thin film on a layered structure;

(b) providing a translucent barrier layer on top of the absorptive coating; and

(c) applying a beam from a laser to an area of the target material;

wherein at least a portion of the absorptive material is vaporized by said beam to form a high pressure plasma which imparts a shockwave on the target metal thin film.

2. The method of claim 1, wherein the beam of said laser is less than 1 millimeter.

3. The method of claim 1, wherein the layered structure is a micro-electromechanical structure.

4. The method of claim 1, further comprising the step of etching the layered structure to create a micro-electromechanical structure.

5. The method of claim 1 performed in a process for manufacturing a micro-electromechanical structure.

6. A method for creating a two-dimensional model of a laser shock peening process which utilizes a laser beam having a predetermined intensity imparted upon a target material that is covered by a absorptive coating and a translucent barrier layer, comprising the steps of:

(a) considering the spatial profile of a laser beam;

(b) considering the radial expansion of plasma generated by a breakdown of material by the laser beam, said material comprising at least one from the group consisting of at least a portion of the absorptive material and at least a portion of the barrier layer; and

(c) creating a model of a LSP process comprising a plurality of layers to determine at least one process parameter by considering at least one of mass conservation, energy conservation and momentum conservation.

7. The method of claim 6, wherein the translucent barrier layer comprises water.

8. A method for characterizing at least one of stress and strain, in at least one direction, for a laser shock processed metal thin film with microscale spatial resolution, comprising the steps of:

(a) determining the curvature of a metal thin film before laser shock peening;

(b) determining the curvature of the metal thin film after laser shock peening;

(c) comparing the curvature of the metal thin film before laser shock peening and the curvature of the metal thin film after laser shock peening to determine a difference; and

(d) determining at least one from the group consisting of average stress and average strain based on the determined difference in curvature between the measurements before laser shock peening and after laser shock peening.

9. A method for characterizing at least one of stress and strain, in at least one direction, for a laser shock peened metal thin film with microscale spatial resolution, comprising the steps of:

(a) monitoring a target metal thin film having a top layer on a single crystal substrate using a fluorescence measurement to determine a surface integrity measurement;

(a) determining a suitable X-ray beam energy level for penetration of the target metal thin film which is greater than a predetermined K absorption edge of the material;

(b) employing an X-ray beam to penetrate the top layer of the target metal thin film;

(c) focusing the incident X-ray beam using a tapered glass capillary to form a microbeam directed on a spot on the target metal thin film;

(d) calibrating the position of a shocked region of the target metal thin film relative to the microbeam;

(d) scanning the target metal thin film relative to the microbeam and recording a diffraction intensity of the single crystal substrate at one or more locations on the target metal thin film using a scintillation detector in a symmetric reflection configuration;

(e) identifying deformations in the substrate of the target metal thin film using X-ray diffraction intensity contrast data; and

(f) determining strain or stress components based on the X-ray diffraction intensity contrast data.

10. The method of claim 9, wherein the spot on the target surface generated by the microbeam is no greater than 10 microns x 10 microns.

11. A method for analyzing hardness of a laser shock treated metal thin film, comprising the steps of:

(a) determining a hardness measurement of a surface of a shock-treated metal thin film at a plurality of points using instrumented nanoindentation;

(b) plotting one or more curves of the determined hardness at a plurality of points; and

(b) determining a residual stress measurement based on the plotted curves.

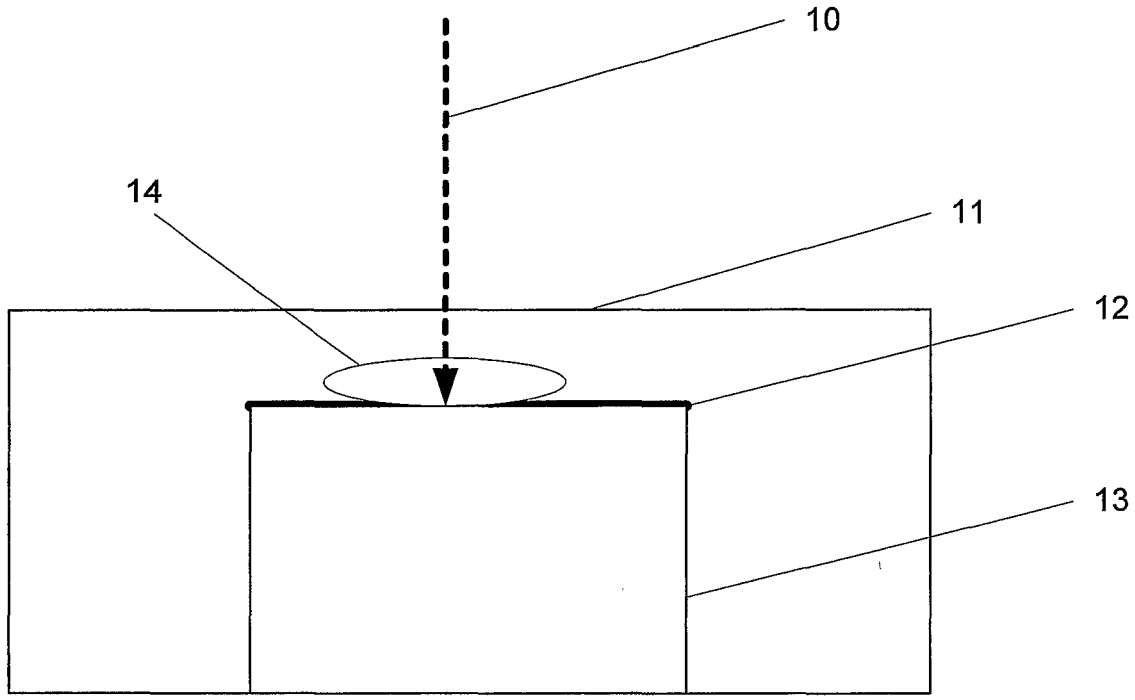

FIG. 1

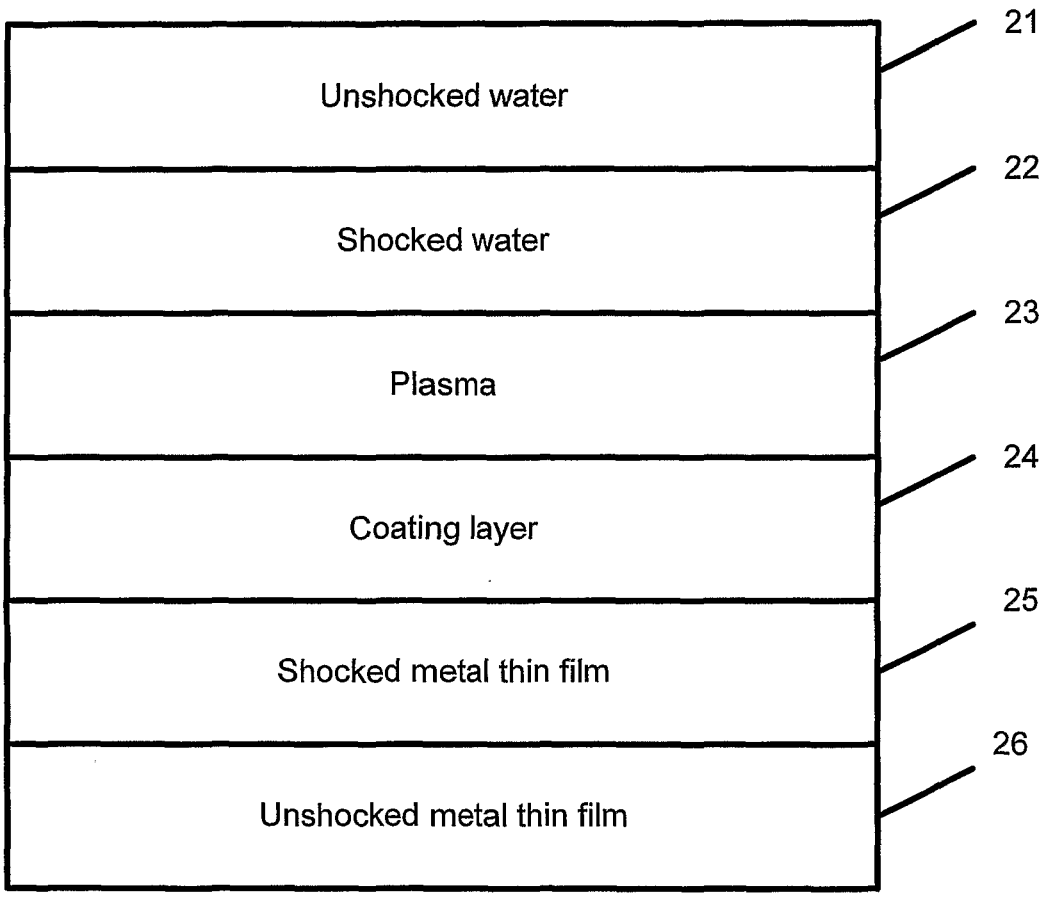
Unshocked water
Shocked water
Plasma
Coating layer
Shocked metal thin film
Unshocked metal thin film
21
22
23
24
25
26

FIG. 2

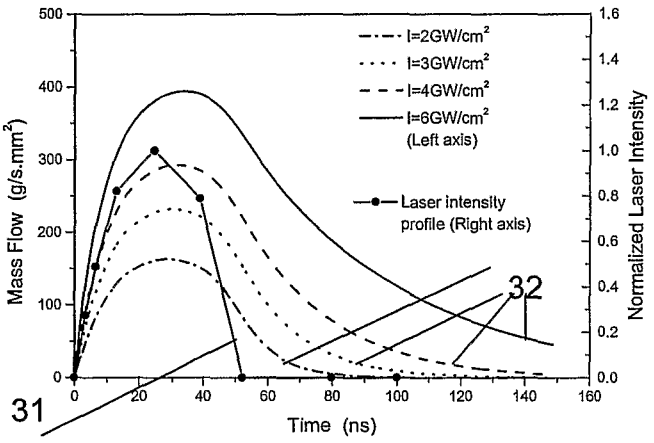
I=2GW/cm²
I=3GW/cm²
I=4GW/cm²
I=6GW/cm²
(Left axis)
Laser intensity profile (Right axis)
Mass Flow (g/s.mm²)
Normalized Laser Intensity
Time (ns)
31
32

FIG. 3

40

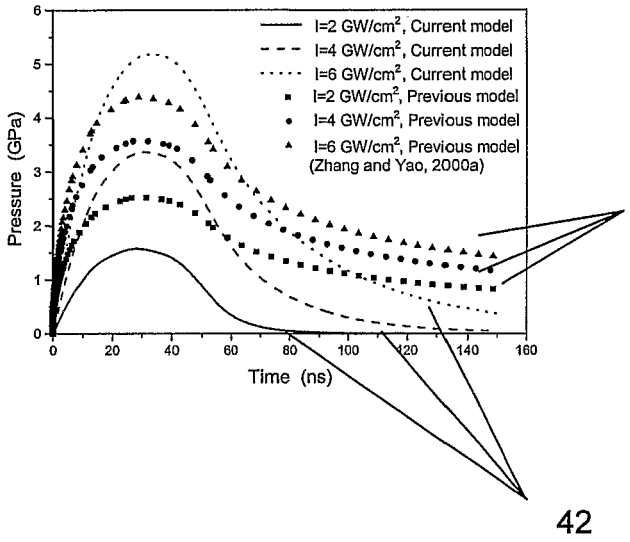
I=2 GW/cm², Current model
I=4 GW/cm², Current model
I=6 GW/cm², Current model
I=2 GW/cm², Previous model
I=4 GW/cm², Previous model
I=6 GW/cm², Previous model
(Zhang and Yao, 2000a)
Pressure (GPa)
Time (ns)
0
1
2
3
4
5
6
0
20
40
60
80
100
120
140
160

41

42

FIG. 4

50

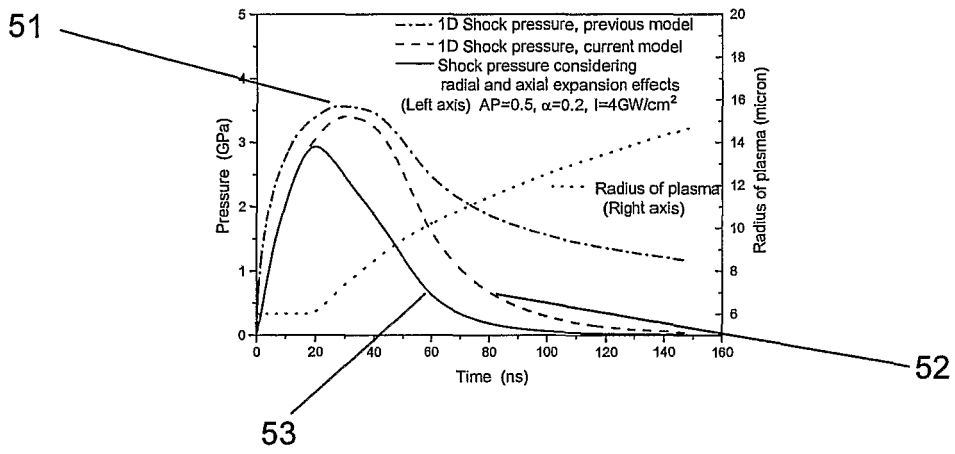
51
1D Shock pressure, previous model
1D Shock pressure, current model
Shock pressure considering
radial and axial expansion effects
(Left axis) AP=0.5, α=0.2, I=4GW/cm²
Radius of plasma
(Right axis)
Pressure (GPa)
Radius of plasma (micron)
Time (ns)
0
20
40
60
80
100
120
140
160
1
2
3
4
5
6
8
10
12
14
16
18
20
52
53

FIG. 5

60

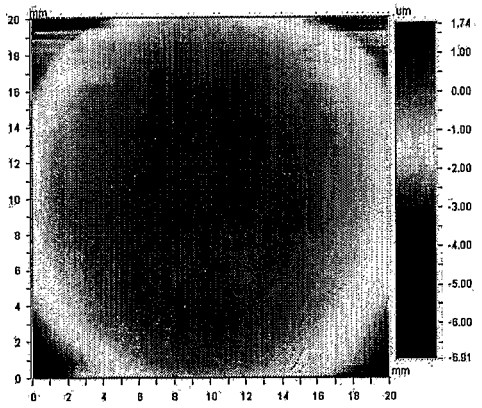
mm
um
1.74
1.00
0.00
-1.00
-2.00
-3.00
-4.00
-5.00
-6.00
-6.91
mm
0
2
4
6
8
10
12
14
16
18
20

FIG. 6

70

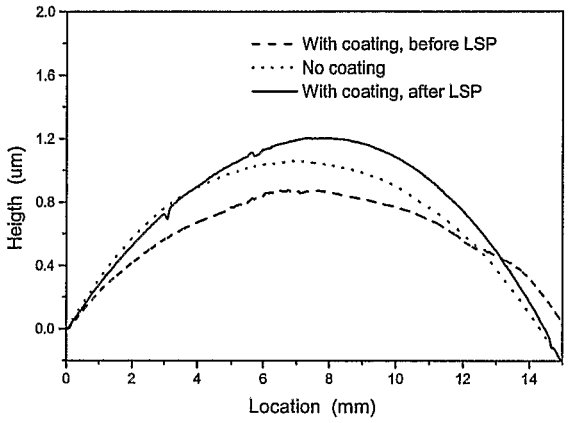
With coating, before LSP
No coating
With coating, after LSP
Heigth (um)
Location (mm)
2.0
1.6
1.2
0.8
0.4
0.0
0
2
4
6
8
10
12
14

FIG. 7

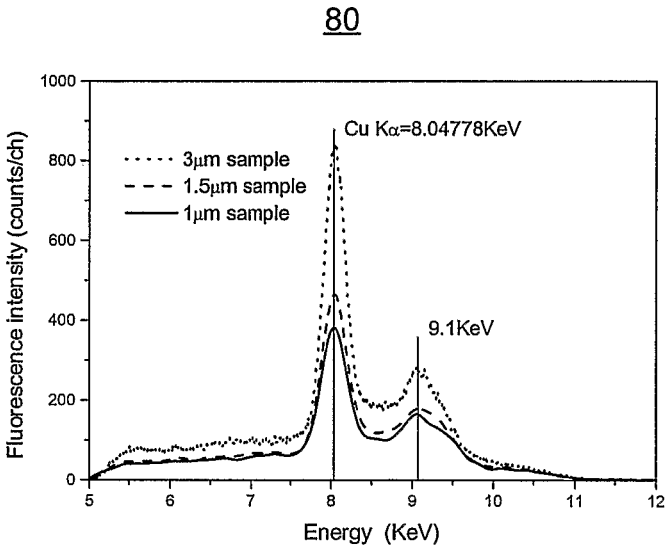
80
1000
800
600
400
200
0
Fluorescence intensity (counts/ch)
3μm sample
1.5μm sample
1μm sample
Cu Kα=8.04778KeV
9.1KeV
5
6
7
8
9
10
11
12
Energy (KeV)

FIG. 8A

81

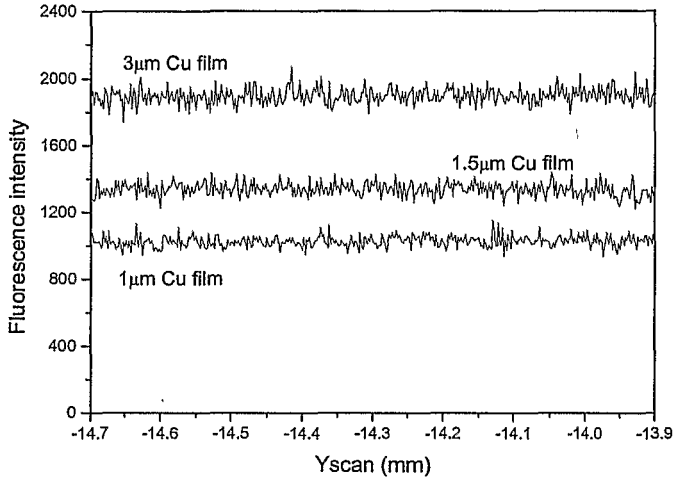
2400
2000
1600
1200
800
400
0
Fluorescence intensity
3μm Cu film
1.5μm Cu film
1μm Cu film
-14.7
-14.6
-14.5
-14.4
-14.3
-14.2
-14.1
-14.0
-13.9
Yscan (mm)

FIG. 8B

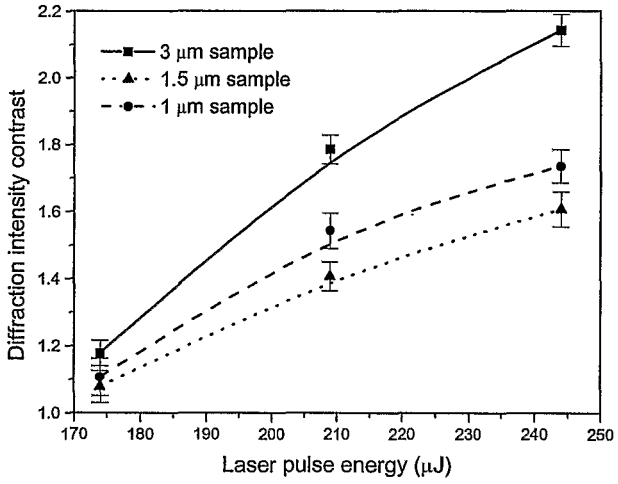
3 μm sample
1.5 μm sample
1 μm sample
Diffraction intensity contrast
Laser pulse energy (μJ)
2.2
2.0
1.8
1.6
1.4
1.2
1.0
170
180
190
200
210
220
230
240
250

FIG. 9

100

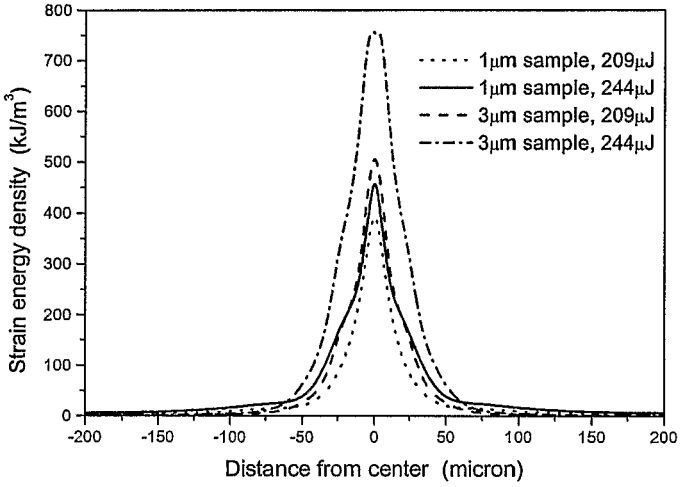
800
700
600
500
400
300
200
100
0
-200
-150
-100
-50
0
50
100
150
200
Strain energy density (kJ/m3)
Distance from center (micron)
1μm sample, 209μJ
1μm sample, 244μJ
3μm sample, 209μJ
3μm sample, 244μJ

FIG. 10

110

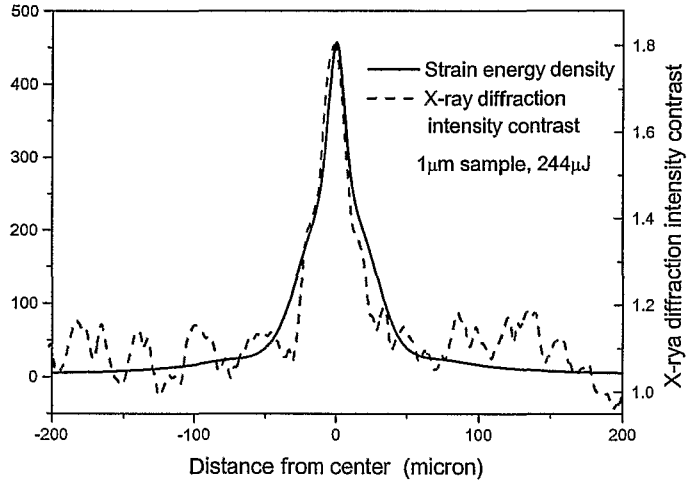
500
400
300
200
100
0
-200
-100
0
100
200
Distance from center (micron)
1.8
1.6
1.4
1.2
1.0
X-rya diffraction intensity contrast
Strain energy density
X-ray diffraction intensity contrast
1μm sample, 244μJ

FIG. 11A

111

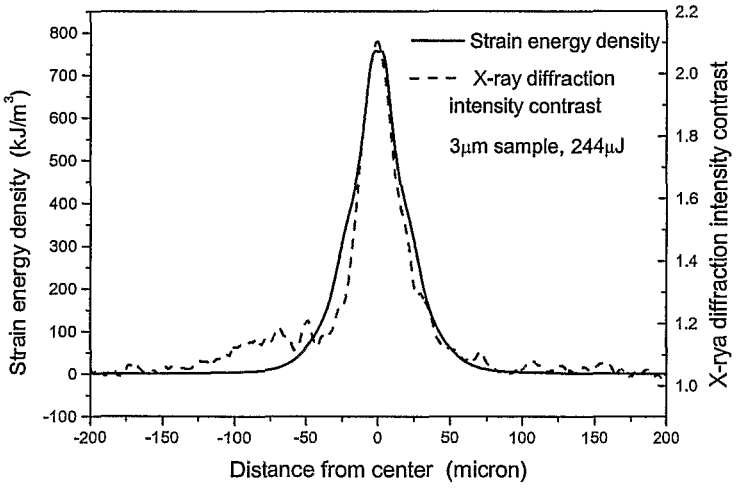
Strain energy density
X-ray diffraction intensity contrast
3μm sample, 244μJ
Strain energy density (kJ/m3)
X-rya diffraction intensity contrast
Distance from center (micron)
800
700
600
500
400
300
200
100
0
-100
2.2
2.0
1.8
1.6
1.4
1.2
1.0
-200
-150
-100
-50
0
50
100
150
200

FIG. 11B

112

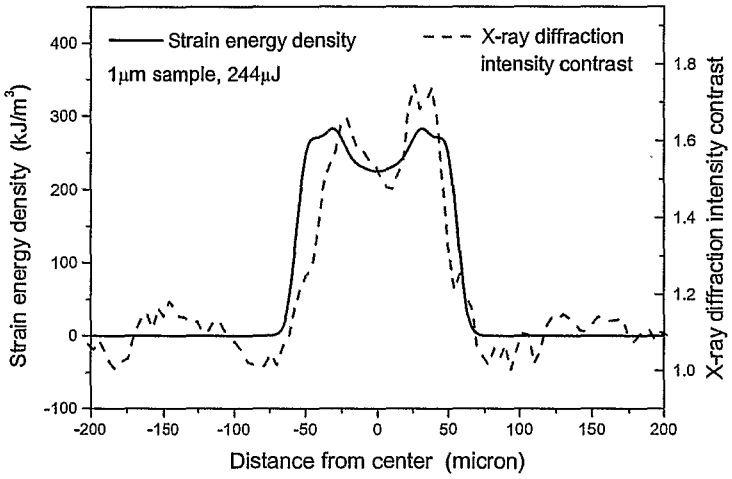
Strain energy density
1μm sample, 244μJ
X-ray diffraction intensity contrast
Strain energy density (kJ/m³)
X-ray diffraction intensity contrast
Distance from center (micron)
400
300
200
100
0
-100
1.8
1.6
1.4
1.2
1.0
-200
-150
-100
-50
0
50
100
150
200

FIG. 11C

120

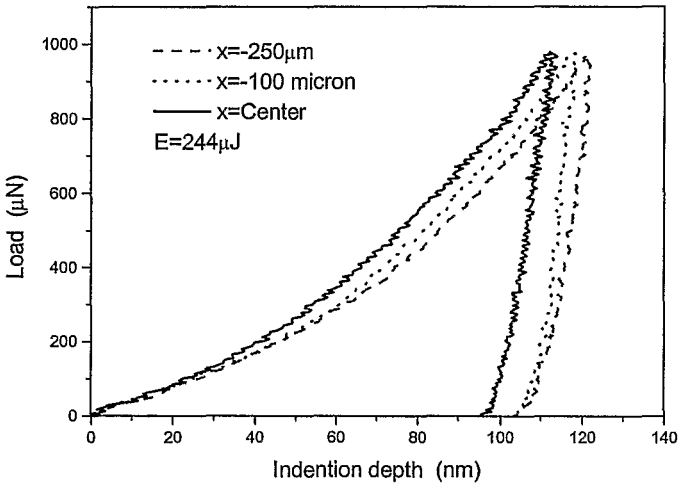
x=-250μm
x=-100 micron
x=Center
E=244μJ
Load (μN)
Indention depth (nm)
0
200
400
600
800
1000
0
20
40
60
80
100
120
140

FIG. 12A

121

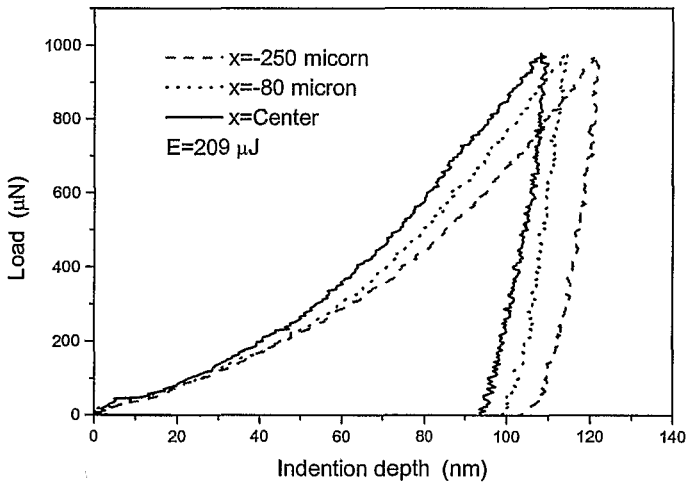
x=-250 micorn
x=-80 micron
x=Center
E=209 μJ
Load (μN)
Indention depth (nm)
0
200
400
600
800
1000
0
20
40
60
80
100
120
140

FIG. 12B

INTERNATIONAL SEARCH REPORT

International application No.
PCT/US03/15701

A. CLASSIFICATION OF SUBJECT MATTER

IPC(7) : B23K 26/00
US CL : 219/121.85

According to International Patent Classification (IPC) or to both national classification and IPC

B. FIELDS SEARCHED

Minimum documentation searched (classification system followed by classification symbols)
U.S. : 219/121.85, 121.6, 121.62121.83

Documentation searched other than minimum documentation to the extent that such documents are included in the fields searched

Electronic data base consulted during the international search (name of data base and, where practicable, search terms used)
US PAT, US PG, Derwent, JPO, EPO, US OCR

C. DOCUMENTS CONSIDERED TO BE RELEVANT

Category *	Citation of document, with indication, where appropriate, of the relevant passages	Relevant to claim No.
X --- Y	US 5,571,575 A (TAKAYANAGI) 5 November 1996 (see relevant sections)	1 --- 2-5
X --- Y	US 5,741,559 A (DULANEY) 21 April 1998 (see relevant sections)	1 --- 2-5
X	US 5,911,891 A (DULANEY et al.) 15 June 1999 (see relevant sections)	8
X	US 6,057,003 A (DULANEY et al.) 2 May 2000 (see relevant sections)	8
X	US 6,144,012 A (DULANEY et al.) 7 November 2000 (see relevant sections)	8

☐ Further documents are listed in the continuation of Box C. ☐ See patent family annex.

* Special categories of cited documents:

"A" document defining the general state of the art which is not considered to be of particular relevance

"E" earlier application or patent published on or after the international filing date

"L" document which may throw doubts on priority claim(s) or which is cited to establish the publication date of another citation or other special reason (as specified)

"O" document referring to an oral disclosure, use, exhibition or other means

"P" document published prior to the international filing date but later than the priority date claimed

"T" later document published after the international filing date or priority date and not in conflict with the application but cited to understand the principle or theory underlying the invention

"X" document of particular relevance; the claimed invention cannot be considered novel or cannot be considered to involve an inventive step when the document is taken alone

"Y" document of particular relevance; the claimed invention cannot be considered to involve an inventive step when the document is combined with one or more other such documents, such combination being obvious to a person skilled in the art

"&" document member of the same patent family

Date of the actual completion of the international search	Date of mailing of the international search report
22 September 2003 (22.09.2003)	09 OCT 2003
Name and mailing address of the ISA/US Mail Stop PCT, Attn: ISA/US Commissioner for Patents P.O. Box 1450 Alexandria, Virginia 22313-1450 Facsimile No. (703)305-3230	Authorized officer Tom Dunn Telephone No. 703-308-0661

Form PCT/ISA/210 (second sheet) (July 1998)